

Water Resources Research

RESEARCH ARTICLE

10.1029/2022WR032943

Lauren J. Sather and Eric J. Roth are joint first authors.

Kev Points:

- Engineered injection and extraction has been demonstrated experimentally and numerical simulations have high spatial correlation
- A novel experimental method is presented to simulate reactive transport at the high-Damköhler number limit
- Results confirm active spreading theory: Reaction increases when the groundwater velocity is perpendicular to the plume interface

Correspondence to:

D. C. Mays, david.mays@ucdenver.edu

Citation:

Sather, L. J., Roth, E. J., Neupauer, R. M., Crimaldi, J. P., & Mays, D. C. (2023). Experiments and simulations on plume spreading by engineered injection and extraction in refractive index matched porous media. *Water Resources Research*, 59, e2022WR032943. https://doi.org/10.1029/2022WR032943

Received 31 MAY 2022 Accepted 20 JAN 2023

Author Contributions:

Conceptualization: Roseanna M. Neupauer, David C. Mays Data curation: Lauren J. Sather, Eric J. Roth, David C. Mays

Funding acquisition: Roseanna M. Neupauer, John P. Crimaldi, David C. Mays Investigation: Eric J. Roth

Methodology: Eric J. Roth Software: Lauren J. Sather Supervision: Roseanna M. Neupauer, John P. Crimaldi Visualization: Eric J. Roth

Writing – original draft: Lauren J. Sather, Eric J. Roth, Roseanna M. Neupauer, David C. Mays Writing – review & editing: Lauren J. Sather, Eric J. Roth, Roseanna M. Neupauer, John P. Crimaldi, David C. Mays

© 2023. American Geophysical Union. All Rights Reserved.

Experiments and Simulations on Plume Spreading by Engineered Injection and Extraction in Refractive Index Matched Porous Media

Lauren J. Sather¹, Eric J. Roth², Roseanna M. Neupauer³, John P. Crimaldi³, and David C. Mays⁴

¹West Yost, Lake Forest, CA, USA, ²Department of Bioengineering, University of Colorado Anschutz Medical Campus, Aurora, CO, USA, ³Department of Civil, Environmental, and Architectural Engineering, University of Colorado Boulder, Boulder, CO, USA, ⁴Department of Civil Engineering, University of Colorado Denver, Denver, CO, USA

Abstract Engineered injection and extraction (EIE) is an in situ groundwater remediation strategy that imposes an engineered spatially and temporally varying velocity field to spread an amendment into the contaminant plume to promote mixing and contaminant degradation through reaction. Here we present a coordinated suite of laboratory experiments and numerical simulations that apply EIE using two pumping sequences: A folding sequence that manipulates plume geometry by stretching and folding, and an oscillating sequence that imposes velocity perpendicular to the plume interface in accordance with previously-reported active spreading theory. Laboratory experiments investigated spreading and mixing of a non-reactive tracer using refractive index matched porous media and laser-induced fluorescence, with remarkable reproducibility between replicates. Numerical simulations matched the experimental results and simulated reactive transport by post-processing sequentially injected non-reactive tracer plumes representing the contaminant and the amendment assuming rapid reaction (i.e., high Damköhler number). This study provides the first experimental verification of EIE using Darcy-scale imaging, demonstrates a novel experimental method to mimic reactive transport at the high-Damköhler number limit, and confirms active spreading theory.

1. Introduction

Reactive transport, the coupled set of processes that control the source, movement, reaction, and fate of solutes in porous media, is fundamental to a range of geophysical processes including soil weathering, element cycling, in-situ mining, and groundwater remediation. Because reactive transport depends on hydrological, microbiological, geochemical, and physical processes, it constitutes a major branch within the broad and interdisciplinary heading of hydrobiogeochemistry (Meile & Scheibe, 2019). Here we focus on physical processes, specifically fluid velocity, on the premise that biogeochemical processes depend on the delivery of reagents and the removal of wastes that are provided almost entirely by fluid advection (Kitanidis, 2012).

A particular motivation for this work is groundwater remediation, the art and science of sequestering or destroying contaminants in aquifers, the geologic structures that store and transmit useful quantities of water for municipal, industrial, and environmental purposes. Groundwater remediation often calls for an amendment to be introduced into the aquifer. Successful in-situ remediation requires that the remediation amendment and contaminant occupy the same pore space, at which point molecular diffusion permits the desired reaction (Kitanidis, 1994). In other words, reaction requires *mixing*, the result of molecular diffusion, which increases the volume into which mass is dissolved and consequently provides dilution. In contrast, *spreading* is defined as solute redistribution by advection, on any scale, without dilution, depending entirely on the velocity field. Spreading enhances mixing by increasing the interfacial area between plumes of differing chemical composition, and by sharpening the concentration gradients at the plume interface, both of which serve to increase mass transport by molecular diffusion (Le Borgne et al., 2010; Villermaux, 2019; Section 2.2). An elegant example of improved remediation through improved spreading has recently been provided by Ye et al. (2021), who used multi-screen wells to inject multiple amendment plumes with correspondingly increased interfacial area. Moreover, spreading takes place at the plume scale, which is an important distinction, because numerical and theoretical studies have shown that different processes dominate at the pore scale versus the plume scale (Jose & Cirpka, 2004).

SATHER ET AL. 1 of 16

Engineered injection and extraction (EIE) is an in situ groundwater remediation strategy that imposes a spatiallyand temporally-varying velocity field to improve spreading, mixing, and reaction. EIE uses a manifold of wells, within and around a contaminant plume, whose injections and extractions create flow fields that manipulate plume geometry to promote reaction while keeping the plume contained within the treatment area. As such, EIE provides a mechanism to apply active spreading in addition to the passive spreading resulting from porous media geometry. Several authors have explored how EIE applies to groundwater remediation. Sposito (2006) simulated pulsed dipole flow, in which alternating injections and extractions were performed through the upper and lower chambers of a well separated by a packer. Bagtzoglou and Oates (2007) simulated pulsed injections and extractions through a manifold of three wells, and Zhang et al. (2009) published a corresponding laboratory study. Lester et al. (2009) simulated the rotating dipole mixer, which imposed a sequence of dipole flows through a manifold of wells placed on a circle, and Cho et al. (2019) published a corresponding field study. Mays and Neupauer (2012) simulated a 12-step process designed to generate plume stretching and folding without re-injection, and Rodríguez-Escales et al. (2017) simulated how this 12-step process could improve degradation of organic compounds during managed aquifer recharge. Asha Farsana et al. (2021) extended the application of the 12-step process to produce three-dimensional chaotic advection by injecting through vertically-separated screened intervals as in Sposito (2006). In each of these cases, EIE controlled plume spreading, demonstrating the promise of active spreading to complement passive spreading in the context of groundwater remediation.

A particularly compelling aspect of EIE is its potential to generate chaotic advection, defined as a laminar flow in which particle separation distances grow exponentially with time, particle trajectories exhibit sensitive dependence on initial conditions, and fluid elements undergo stretching and folding (Aref et al., 2017; Ottino, 1989; Speetjens et al., 2021). A subset of the groundwater remediation EIE studies cited above have flows for which chaotic advection has been demonstrated (Lester et al., 2009; Mays & Neupauer, 2012; Sposito, 2006), so in these cases, EIE constitutes one application of the larger literature on chaotic advection (e.g., Aref et al., 2017; Ottino, 1989; Speetjens et al., 2021). Moreover, there is evidence that even natural flows can manifest chaotic advection (Lester et al., 2013; Trefry et al., 2019).

Along these lines, our group has studied several aspects of EIE within the framework of chaotic advection, including a theoretical demonstration of chaotic advection by stretching and folding (Mays & Neupauer, 2012), a discussion of the practical and regulatory benefits of avoiding re-injection (Mays & Neupauer, 2013), and simulations demonstrating how aquifer heterogeneity increases spreading and changes the nature of chaotic advection (Neupauer et al., 2014). Simulations indicated that chaotic advection accelerates contaminant degradation (Piscopo et al., 2013). Each of these studies used the same 12-step pumping sequence, but subsequent work showed that sorbing contaminants require different pumping sequences (Neupauer & Mays, 2015). Notably, multi-objective evolutionary algorithms identified that the optimal pumping sequence for non-sorbing contaminants (Piscopo et al., 2015) and sorbing contaminants (Piscopo et al., 2016) were generally *not* those that imposed chaotic advection. Importantly, these works were theoretical, not experimental. Filling this experimental gap is the first, and perhaps most important, contribution of the present study.

Except for one laboratory study (Zhang et al., 2009) and one field study (Cho et al., 2019), there has been no other direct experimental evidence for plume spreading by EIE, with or without chaotic advection. The remainder of the EIE literature is modeling, so no previous study has had the ability to demonstrate the efficacy of EIE in a physical system with dispersion. This last point is important for the following reason: Though pore-scale physics can be modeled with the Navier-Stokes equation and molecular diffusion theory, the practical execution of such a conceptual model is unreasonable due to the complicated, and typically immeasurable, network of no-flow boundary conditions introduced by the geometry of the porous media (Stöhr et al., 2003). Consequently, laboratory experiments are needed to calibrate and verify models by providing data that has been influenced by physical pore-scale dispersion. Indeed, recent reviews have emphasized the need for experimental studies (Speetjens et al., 2021; Valocchi et al., 2019).

Here we present a coordinated suite of laboratory experiments and numerical simulations that apply EIE using two pumping sequences. Section 2 describes the conceptual model (including the pumping sequences), the laboratory experiments, and the numerical simulations. Section 3 presents results emphasizing the reproducibility of experimental replicates and remarkably high spatial correlation between experiments and simulations, while Section 4 highlights three new contributions, specifically (a) presentation of a new window through which to measure how solute plumes interact in porous media, (b) demonstration of a novel single-tracer experimental

SATHER ET AL. 2 of 16

19447973, 2023, 2, Downloaded

method to mimic reactive transport, and (c) explanation of how velocity fields, plume interfaces, and longitudinal dispersion work in concert to determine reactive transport.

2. Methods

This section describes the conceptual model, the experimental methods, the numerical methods (incorporating experimental data), and an experimental procedure that uses two sequential experiments with different initial configurations of a single dye (called "two-solute experiments") as input to a numerical simulation designed to mimic reactive transport under conditions of high Damköhler number (fast reaction). Additional details of the experimental and numerical methods are provided in the dissertations of Roth (2018) and Sather (nee Reising, 2018), respectively.

2.1. Conceptual Model

This study comprises single-solute and two-solute experiments and simulations, where the single-solute experiments and simulations represent non-reactive transport (i.e., conservative transport) and the two-solute experiments and simulations represent reactive transport of contaminant A and remediation amendment B, both of which are aqueous and non-sorbing. For two-solute reactive transport, the chemical reaction takes the form of a bimolecular reaction, given by $A + B \rightarrow P$; thus, reaction rates $R_A = R_B = -R_P = kC_AC_B$, where k is the reaction rate coefficient and C_A and C_B are the concentrations of the contaminant and amendment, respectively. We assume that the reaction is fast relative to the transport time scale, thus $k \rightarrow \infty$. Because the dimensionless Damköhler number, Da, is the ratio of reaction rate to transport rate, this assumption corresponds to the high-Damköhler limit, which for practical purposes means Da > 100 (Sanchez-Vila et al., 2007). In the context of groundwater remediation, an example remediation reaction at the high-Damköhler limit is in situ chemical oxidation (ISCO) of organic contaminants with the permanganate anion MnO_4^- (e.g., Cha & Borden, 2012). For the single-solute experiments and simulations of non-reactive transport, $R_i = 0$. Product P is assumed to be aqueous and non-clogging.

The experiments are conducted in the apparatus shown in Figure 1, which features quasi-two-dimensional flow through a rectangular aquifer of constant thickness. This apparatus was designed to represent a confined, two-dimensional, isotropic rectangular aquifer with no-flow boundaries on all sides. For the single-solute (non-reactive) scenario, an approximately circular solute plume is initially centered at the origin. For the two-solute (reactive) scenario, the initial distributions of solutes A and B form concentric circular plumes centered at the origin, with an approximately circular plume of solute B surrounded by an approximately annular plume of solute A. Four wells are placed symmetrically around the plume, each at a distance of L from the origin and screened over the entire thickness of the apparatus. A fifth well is located at the origin.

The wells are pumped according to two different EIE sequences, where each sequence comprises several steps, and each step includes at least one injection well and at least one extraction well such that the net injection rate was always zero. Having net-zero injection was a practical necessity for the laboratory experiments, which were conducted in saturated porous media with specified flow boundary conditions, and consequently did not allow volume imbalance between injections and extractions. Following precedence by previous researchers (e.g., Jones & Aref, 1988; Sposito, 2006, Mays & Neupauer, 2012), injection and extraction volumes are nondimensionalized by dividing by the pore volume, where a pore volume is defined as the fluid contained within a cylinder, centered at the origin, with radius L = 11.6 cm, thickness b = 4.3 cm (i.e., the apparatus thickness), and a spatially averaged porosity of n = 0.311, which is the measured average porosity in the experiment (Roth et al., 2021).

The first EIE sequence, shown in Table 1, is called the folding sequence. This sequence was chosen to implement Ottino's (1989) stretching-and-folding paradigm for optimizing plume spreading in laminar flow. The second EIE sequence, shown in Table 2, is called the oscillating sequence. This sequence was chosen to exploit the findings of Sather et al. (2022), who showed that active spreading, and therefore reaction, is highest where the local velocity is generally perpendicular to the plume interface.

2.2. Laboratory Experiments

This section will briefly recapitulate the experimental methods described elsewhere (Roth et al., 2020, 2021). Experiments were conducted in a quasi-two dimensional flow cell with dimensions of $49.2 \times 49.2 \times 4.3 \text{ cm}^3$

SATHER ET AL. 3 of 16

1944/7973, 2023, 2, Downloaded from https://agupubs.onlinelibrary.wiley.com/doi/10.1029/2022WR032943 by University Of Colorado, Wiley Online Library on [06/02/2023]. See the Terms

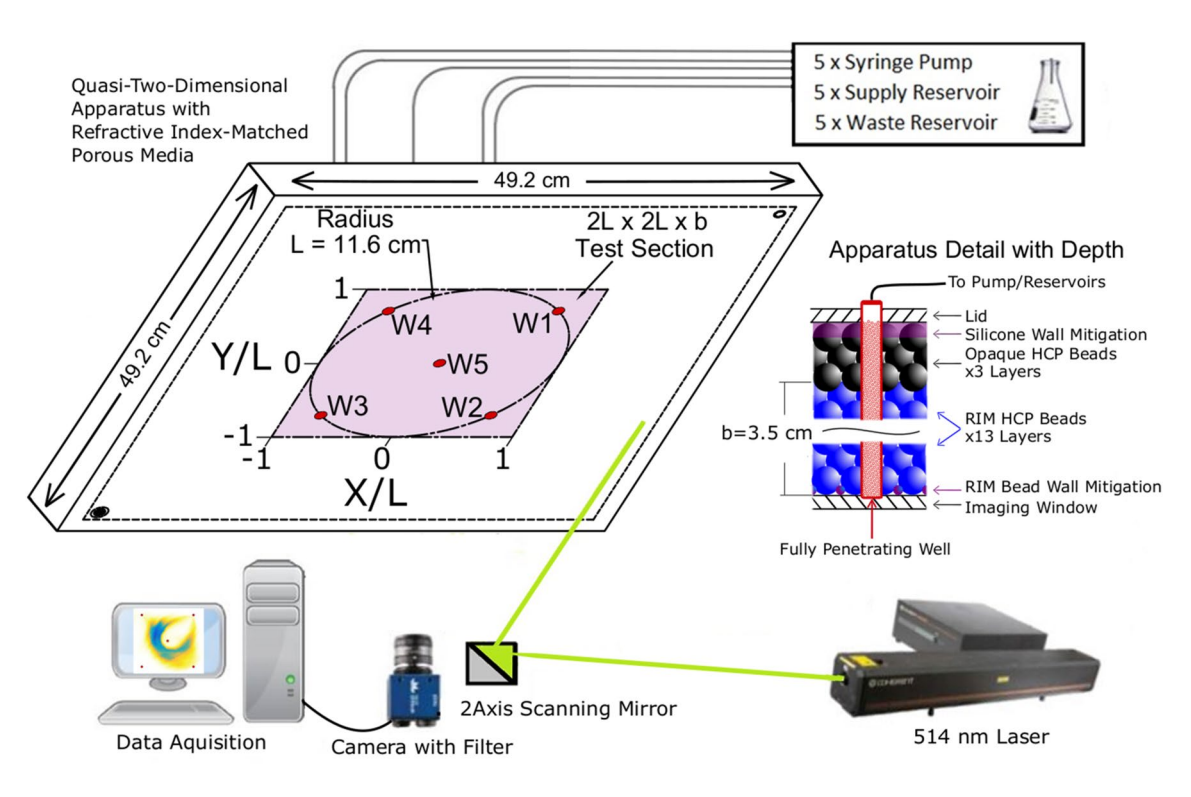


Figure 1. Dimensional schematic of the engineered injection and extraction (EIE) apparatus with detail of bead packing over depth. Opaque HCP beads (black), RIM HCP bulk porous media (blue), and wall effect mitigation (red). Note the $2L \times 2L \times b$ test section corresponding to the region of interest for data presented in this article, as well as the orientation of wells 1–5 (W1–W5).

(Figure 1). The flow cell contained five fully screened injection/extraction wells that penetrated the entire 4.3 cm thickness of the cell to create two-dimensional flow. The apparatus was filled with approximately homogeneous, hexagonal-close-packed (HCP), spherical, monodisperse porous media (3 mm borosilicate glass beads, Pyrex, part# 7268-3), that was refractive index matched (RIM) with glycerin, the pore fluid (99.7% USP glycerin, Chemworld, CAS# 56-81-5). Rhodamine 6G dye (Aldrich, CAS# 989-38-8) was used as the solute.

The Péclet number will vary with velocity, from a maximum near the active wells to a minimum far from the active wells. The order of magnitude depends on whether we define the Péclet number with respect to molecular diffusion, $D_{\rm m}$, or hydrodynamic dispersion, $D_{\rm m}$. If we use $D_{\rm m}=1.9\times10^{-9}~{\rm cm^2/s}$ for rhodamine dye in glycerin, and the porous media diameter for L, then the Péclet number $Pe=vL/D_{\rm m}\approx10^6$ near the injection well. This confirms the conventional wisdom, in porous media research, that advection dominates molecular diffusion; this is especially true in our case given the small molecular diffusion of rhodamine in glycerin. On the other hand, if we use $D=\alpha_L v$ for longitudinal hydrodynamic dispersion, then velocity appears in both the numerator and the denominator of the Péclet number $Pe=vL/D=L/\alpha_L=(3~{\rm mm})/(2~{\rm mm})=1.5$. This result indicates that advection and dispersion are in balance for our experiments.

Table 1 Pore Volumes Injected Per Step in the Folding Sequence									
	Well 1	Well 2	Well 3	Well 4	Well 5				
Step 1	0	0.277	0	-0.277	0				
Step 2	0	-0.555	0	0.444	0.111				
Step 3	0.139	-0.028	0.139	-0.250	0				
Step 4	0.277	0	-0.277	0	0				

0.257

Step 5

-0.428

During the experiment, the dye distribution was imaged through the bottom wall of the apparatus (Figure 1) using novel experimental methods to mitigate wall effects (Roth et al., 2020) and to image plume deformation using laser-induced fluorescence (Roth et al., 2021). The bottom of the cell was illuminated by a 514 nm laser (Coherent, Innova 90C-6) whose beam was scanned progressively over the imaging area for a duration of 1 second per scan by using two scanning mirrors (Thorlabs, GVS312). The camera (Imperx, Bobcat ICL-B1410M-SCO), located next to the scanning mirrors, captured images from the same side as the incident light. An optical bandpass filter (Omega Optics, 555DF30), was attached to the camera lens, blocking the 514 nm excitation light from the laser while transmitting fluoresced

SATHER ET AL. 4 of 16

0.171

19447973, 2023, 2, Downloaded from https://agup

doi/10.1029/2022WR032943 by University Of Colorado,

 Table 2

 Pore Volumes Injected Per Step in the Oscillating Sequence

Well 1 Well 2 Well 3 Well 4 Well 5 Step 1 0 -0.0505 0 -0.0505 0.101 Step 2 0.101 -0.101 0.101 -0.101 0 Step 3 -0.101 0 0.101 0 0 Step 4 0.202 0 -0.202 0 0 Step 5 -0.202 0 0.202 0 0	Tore volumes injected for step in the Oscillating Sequence								
Step 2 0.101 -0.101 0.101 -0.101 0 Step 3 -0.101 0 0.101 0 0 Step 4 0.202 0 -0.202 0 0		Well 1	Well 2	Well 3	Well 4	Well 5			
Step 3 -0.101 0 0.101 0 0 Step 4 0.202 0 -0.202 0 0	Step 1	0	-0.0505	0	-0.0505	0.101			
Step 4 0.202 0 -0.202 0 0	Step 2	0.101	-0.101	0.101	-0.101	0			
•	Step 3	-0.101	0	0.101	0	0			
Step 5 -0.202 0 0.202 0 0	Step 4	0.202	0	-0.202	0	0			
	Step 5	-0.202	0	0.202	0	0			

light from the dye used for plume visualization. To our knowledge, these were the first Darcy-scale measurements of plume deformation during EIE in RIM porous media.

The experimental apparatus was designed to make Darcy-scale rather than pore-scale measurements. Therefore, measurements were averaged vertically through 13 layers of 3 mm HCP beads. The top and bottom walls of the cell (parallel to flow) used a novel wall effect mitigation technique to eliminate preferential flows at apparatus walls (Roth et al., 2020). Briefly, wall effect mitigation techniques make the porosity at the wall equal to the porosity in the bulk porous media. By having uniform porosity through the entire depth of porous media, velocity is also vertically uniform. To allow optical access

across the bottom wall of the apparatus, a layer of RIM beads, whose diameter is $\frac{1}{3}$ the diameter of the regular 3 mm beads, is placed within the void space at the wall. The top wall requires no optical access, so uniform porosity was imposed by embedding the top layer of beads in a half-bead-diameter depth layer of silicone, which made the effective aquifer thickness b = 4.3 cm (Table 3). To further ensure uniform flow through the imaging depth, three layers of opaque HCP beads are placed just below the top wall. By adding this opaque layer, any flow irregularities near the top wall will not be included in the data, leaving an imaging depth of 3.5 cm (13 HCP bead layers). Side walls have no wall effect mitigation. Therefore, only a $2L \times 2L \times b$ (23.2 \times 23.2 \times 3.5 cm³) test section is considered for data analysis (Figure 1).

Table 3 *Modeling Parameters*

Parameter	Value
Average hydraulic conductivity, K	0.1663 cm/min
Aquifer thickness, b	4.3 cm
Specific storage, S_s	$9.3 \times 10^{-7} \text{ 1/cm}$
Average porosity, n	0.311
Aquifer west boundary, x_w	−25 cm
Aquifer east boundary, x_e	25 cm
Aquifer north boundary, y_n	25 cm
Aquifer south boundary, y_s	−25 cm
Finite difference grid discretization	0.05 cm
Coordinates of well 1, x ₁	(8.2 cm, 8.2 cm)
Coordinates of well 2, $\mathbf{x_2}$	(8.2 cm, -8.2 cm)
Coordinates of well 3, x ₃	(-8.2 cm, -8.2 cm)
Coordinates of well 4, x ₄	(-8.2 cm, 8.2 cm)
Coordinates of well 5, $\mathbf{x_5}$	(0 cm, 0 cm)
Distance between wells, L	11.6 cm
Injection/extraction step duration	30 min
Longitudinal dispersivity, α_L	0.2 cm
Transverse dispersivity, α_T	0.02 cm
Initial concentration of solute A, C_{A0}	0.25 mg/mL
Initial concentration of solute B, C_{B0}	1 mg/mL
Radius of initial plume of solute A, r_A	1.933 cm
Outer radius of initial plume of solute B, r_B	3.97 cm
Number of particles of solute A	3×10^{6}
Number of particles of solute B	1×10^{6}

Flow was supplied by a plumbing system containing five high accuracy syringe pumps (KD Scientific, Legato 270), feeding the wells from the top of the cell (Figure 1) over a fixed step duration of 30 min. Prior to the experiment, the packed EIE cell was saturated with glycerin. A 20 mL volume of a solution of 8 mg/L Rhodamine 6G dye (Aldrich, CAS# 989-38-8) dissolved in glycerin was then injected through the center well and imaged to record the initial condition. One of the EIE sequences described above would then be performed with images of plume evolution captured every 15 s (i.e., 120 images per step). For example, the first step of the folding sequence (Table 1), simultaneous injection and extraction 0.277 pore volumes corresponds to a discharge of approximately Q = 5.2 mL/min for 30 min, where the pore volume $\pi nbL^2 = 565$ mL. Two replicate experiments were performed for the folding sequence (Table 1). As discussed below, these replicates were practically identical, so only one replicate was performed for the oscillating sequence (Table 2). Upon completion of the EIE sequence, all dye was extracted from the cell through the center well while supplying dye-free glycerin to the surrounding wells. This allowed the saturated porous media bed to be used for subsequent EIE experiments. Upon completion of all experiments, all of which used the same porous media bed, the EIE cell was completely flooded with dye and imaged. The dye-saturated image was then used to create a porosity map as shown in Figure 4 of Roth et al. (2021).

2.3. Numerical Simulations

Numerical simulations of glycerin flow and dye (solute) transport were conducted to match the results of the laboratory experiments. The governing equation of the transient flow for this porous medium is given by

$$S_s \frac{\partial h}{\partial t} = \nabla \cdot K \nabla h + \sum_{j=1}^5 Q_j(t) \delta(\mathbf{x} - \mathbf{x}_j), \tag{1}$$

where S_s is specific storage, h is hydraulic head, t is time, K is the hydraulic conductivity (here assumed to be isotropic), Q_j is the injection rate per unit aquifer thickness in well j, $\mathbf{x} = (x, y)$ is the spatial coordinate, \mathbf{x}_j is the location of well j, and $\delta()$ is the Dirac delta function. Because the media are

SATHER ET AL. 5 of 16

monodisperse spheres with nearly homogeneous porosity, the hydraulic conductivity is also nearly homogeneous. The slight variability of K is modeled as $K = k\rho g/\mu$, where $k = n^3 d^2/[180(1-n)^2]$ is the permeability estimated with the Kozeny-Carman equation using bead diameter d = 3 mm, $\rho = 1.25$ g/cm³ is the density of glycerin, g = 980 cm/s² is the acceleration of gravity, and $\mu = 14$ g/(cm·s) is the dynamic viscosity of glycerin. The boundary conditions are

$$\nabla h \cdot \mathbf{n} = 0 \text{ at } x = x_w, x = x_e, y = y_n, y = y_s,$$
(2)

where **n** is the outward unit normal vector, x_w , x_e , y_n , and y_s are the coordinates of the west, east, north, and south boundaries, respectively. The initial condition is $h = h_o$ for all **x**. The flow Equation 1 is solved numerically using MODFLOW-2005, a standard finite difference groundwater flow simulator (Harbaugh et al., 2017). The flow model in MODFLOW used a grid of $1,045 \times 1,045$ cells, each of which was 0.48×0.48 mm². Parameter values are given in Table 3.

The numerical simulations comprise single-solute and two-solute simulations, where the single-solute simulations represent non-reactive transport based on a single injected plume of Rhodamine dye and the two-solute simulations represent reactive transport of contaminant A and remediation amendment B, both of which are aqueous and non-sorbing, based on sequentially injected plumes of Rhodamine dye with different initial configurations. The transport of a dissolved solute in porous media is governed by the advection-dispersion-reaction equation (ADRE), given by

$$n\frac{\partial C_i}{\partial t} = -\nabla \cdot (n\mathbf{v}C_i) + \nabla \cdot \mathbf{D}n\nabla C_i - nR_i, \tag{3}$$

where C_i is the concentration of solute i, (i = A for the contaminant, i = B for the amendment, and i = P for the reaction product), t is time, R_i is the reaction rate of solute i, n is porosity whose slight spatial variation is taken from the porosity map, \mathbf{v} is the groundwater velocity vector from Darcy's law, $\mathbf{v} = -(K/n)\nabla h$, and \mathbf{D} is the dispersion tensor, with components given by

$$D_{xx} = \alpha_L \frac{v_x^2}{|\mathbf{v}|} + \alpha_T \frac{v_y^2}{|\mathbf{v}|},$$

$$D_{xy} = D_{yx} = (\alpha_L - \alpha_T) \frac{v_x v_y}{|\mathbf{v}|},$$

$$D_{yy} = \alpha_L \frac{v_y^2}{|\mathbf{v}|} + \alpha_T \frac{v_x^2}{|\mathbf{v}|},$$
(4)

where α_L and α_T are the hydrodynamic dispersivities in the longitudinal and horizontal transverse directions, respectively, with $\alpha_L > \alpha_T$, v_x and v_y are the x- and y-components of velocity, respectively, and the vertical bars denote magnitude. The boundary conditions on C are

$$\nabla C_i \cdot \mathbf{n} = 0 \text{ at } x = x_w, x = x_e, y = y_n, y = y_s.$$
 (5)

The initial solute distributions of the reactants A and B are created to match the initial dye distribution in the experiment, and the initial condition of reaction product P is $C_P = 0$. If solutes A and B react instantaneously to form the reaction product P with reaction rates $R_A = R_B = -R_P = kC_AC_B$, then the mass of A is conserved (as A alone or as part of P) and the mass of B is conserved (as B alone or as part of P) (Gramling et al., 2002). Thus, Equation 3 can be rewritten in terms of the concentrations $C_{A+P} = C_A + C_P$ and $C_{B+P} = C_B + C_P$, as

$$n\frac{\partial C_{A+P}}{\partial t} = -\nabla \cdot (n\mathbf{v}C_{A+P}) + \nabla \cdot \mathbf{D}n\nabla C_{A+P},\tag{6}$$

and

$$n\frac{\partial C_{B+P}}{\partial t} = -\nabla \cdot (n\mathbf{v}C_{B+P}) + \nabla \cdot \mathbf{D}n\nabla C_{B+P},\tag{7}$$

which eliminates the reaction terms. The boundary conditions are still defined as in Equation 5, and the initial conditions are still equivalent to the initial dye distribution in the experiment. The concentrations of each solute

SATHER ET AL. 6 of 16

19447973, 2023, 2, Downloaded from https://agupubs.onlinelibrary.wiley.com/doi/10.1029/2022WR032943 by University Of Colorado

Table 4Correlation Coefficients for Single-Solute Simulations and Experiments of Non-Reactive Transport

	Initial condition	Step 1	Step 2	Step 3	Step 4	Step 5
Folding Sequence Experimental Replicate 1 versus Replicate 2	0.99	0.99	0.99	0.99	0.99	0.99
Folding Sequence Experimental Replicate 1 versus Numerical	1.00	0.96	0.94	0.96	0.96	0.96
Folding Sequence Experimental Replicate 2 versus Numerical	1.00	0.97	0.95	0.97	0.96	0.96
Oscillating Sequence Experiment versus Numerical	1.00	0.96	0.97	0.96	0.96	0.96

can be recovered from the solutions to Equations 6 and 7 as follows. Since the reaction is assumed to occur instantaneously, solute A and B cannot co-exist. For simplicity, we assume the reaction has a 1:1 mass ratio and 1:1 stoichiometric ratio of A and B. Thus, wherever C_{A+P} and C_{B+P} co-exist, equal masses of solute A and B react until the limiting reactant is completely converted to reaction product P, such that the mass of P is twice the mass of P (or P) that reacted. Mathematically, the concentrations of each solute are given by Gramling et al. (2002)

$$C_{\mathbf{P}}(\mathbf{x},t) = 2\min[C_{\mathbf{A}+\mathbf{P}}(\mathbf{x},t), C_{\mathbf{B}+\mathbf{P}}(\mathbf{x},t)]$$
(8)

$$C_{\mathbf{A}}(\mathbf{x},t) = C_{\mathbf{A}+\mathbf{P}}(\mathbf{x},t) - C_{\mathbf{P}}(\mathbf{x},t)/2 \tag{9}$$

$$C_{\rm B}(\mathbf{x},t) = C_{\rm B+P}(\mathbf{x},t) - C_{\rm P}(\mathbf{x},t)/2$$
 (10)

Initial conditions for each pumping sequence were created by inserting particles into the domain that matched the concentration distribution of the experiments. For reactive simulations only, additional particles were placed inside the well to simulate dye within the well that was not measured in the experiment. The transport Equations 6 and 7 are solved numerically using RW3D (Salamon et al., 2006), which uses random walk particle tracking. Particle tracking is a common method for modeling solute transport in aquifers known for its computational efficiency and absence of numerical dispersion (Berkowitz et al., 2006; Le Borgne et al., 2008a, 2008b). The transport model in RW3D used the same grid as the flow model in MODFLOW (1,045 × 1,045 cells of 0.48 × 0.48 mm²) with velocities calculated from heads at the center of each cell. Dispersion was modeled via particle tracking, so there was no grid for dispersion. Then concentrations were determined from particle positions imposed onto the grid. The time step for the transport simulation was 0.1 min. The longitudinal dispersivity coefficient (Table 3) was fitted to maximize the two-dimensional spatial correlation between simulations and one-solute experiments reported in Table 4, and the transverse dispersivity was assumed to be 1/10 of the longitudinal dispersivity. For the non-reactive transport simulations, the bivariate density estimation model from the R package locfit produced smooth concentration fields from the particle positions provided by RW3D (Loader, 2013). For the reactive transport simulations, the particle positions and masses provided by RW3D were first used to calculate a concentration field by binning the particles. This concentration field was then smoothed using a bivariate local likelihood regression model from locfit.

2.4. Plume Comparison Methods

Several methods are available to compare numerically simulated plumes and experimentally measured plumes (Roth et al., 2021): Comparison of plume location using centroid locations, comparison of plume spreading using moments of inertia, comparison of dilution using the reactor ratio of Kitanidis (1994), and comparison of plume geometry using the two-dimensional correlation coefficient. Since each of these comparison metrics give similar results (Roth, 2018), the current study compares plumes using the two-dimensional correlation coefficient, ρ , given by

$$\rho = \frac{\sum_{i} \sum_{j} \left[C^{1}(x_{i}, y_{j}) - \overline{C^{1}} \right] \left[C^{2}(x_{i}, y_{j}) - \overline{C^{2}} \right]}{\sqrt{\left\{ \sum_{i} \sum_{j} \left[C^{1}(x_{i}, y_{j}) - \overline{C^{1}} \right]^{2} \right\} \left\{ \sum_{i} \sum_{j} \left[C^{2}(x_{i}, y_{j}) - \overline{C^{2}} \right]^{2} \right\}}},$$
(11)

SATHER ET AL. 7 of 16

1944/973, 2023, 2, Downloaded from https://agupubs.onlinelibrary.wiley.com/doi/10.1029/2022WR032943 by University Of Colorado, Wiley Online Library on [06/02/2023]. See the Terms

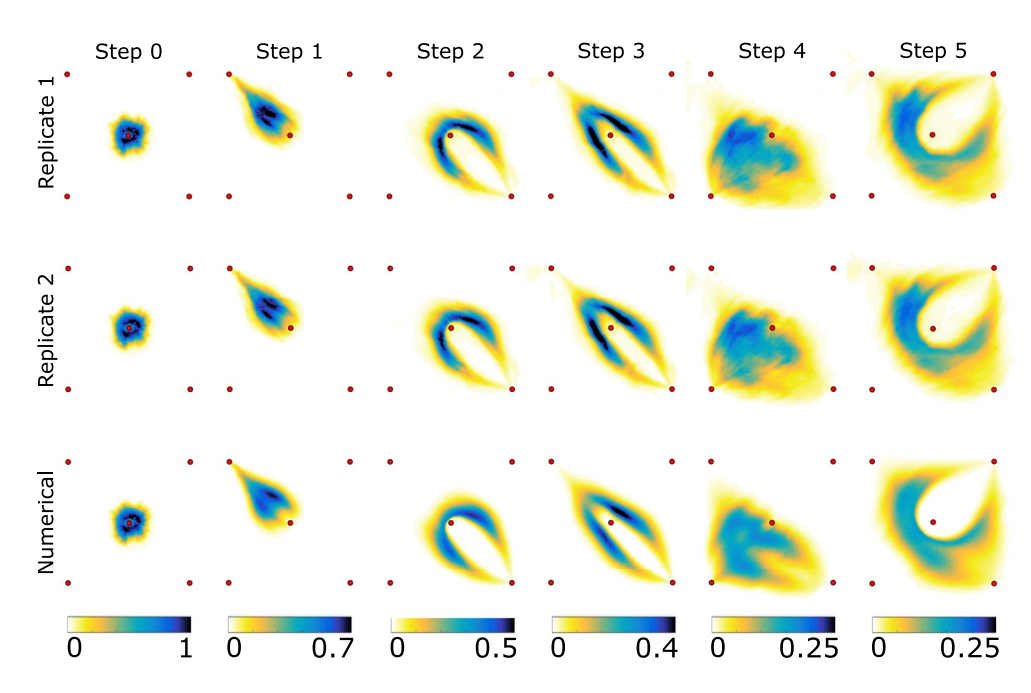


Figure 2. Experimental replicates and numerical plume images of C/C_o for the folding sequence. Small red circles represent wells (refer to Figure 1 for spatial scale). The numerical results match the experimental results with a high two-dimensional correlation (Table 5). The top two rows are reproduced from Roth et al. (2021) with permission from Springer Nature.

where C^1 and C^2 are the concentrations of the first and second data set used in the comparison. Equation 11 was evaluated using the corr2 function in Matlab.

2.5. Two-Solute Experimental Technique for Simulated Reactive Transport

An experimental protocol valid for instantaneous reaction (i.e., high Damköhler number) was developed to use a single dye to investigate the simultaneous transport of two solutes, as would occur during, for example, in-situ remediation of contaminated groundwater. The transport of two solutes is investigated by performing two different experiments, where each solute plume has its own initial condition, but subsequently both plumes undergo the same EIE sequence (Table 1) within the same media packing. One solute plume represents A + P and the other represents B + P. The experimental procedure for this technique follows that described above, except for the introduction of the dye plume. For the single-solute experiments, 20 mL of dye solution was injected into the center well. For the experiment of the transport of B + P, half this volume (i.e., 10 mL) of the dye solution was injected into the center well to create the approximately circular inner plume of the concentric circular plumes. For the experiment of the transport of A + P, 10 mL of dye was injected at the center well, followed by an injection of 10 mL of undyed glycerin. This created the outer plume of the approximately concentric circular plumes. The total volume of dye solution in these two experiments is equal to the volume of dye solution used in a particular single-solute experiment.

Because the experimental results were highly reproducible (see next section), the images of the two solute plumes from the two different experiments can be superimposed to mimic the behavior of the two plumes in the same flow field. Thus, we track the movement of two non-reactive solutes, A + P and B + P, in the two experiments, and we convert these to concentrations of A, B, and B using Equations 8–10 during image processing.

3. Results

For the folding sequence, experimental results for two replicates and corresponding simulations are shown in Figure 2. This figure plots the vertically averaged (i.e., quasi-two dimensional) spatial distribution of solute concentration after each of the five steps in Table 1. The initial plume is approximately circular, with deviations resulting from the slight heterogeneity because of slight non-uniformity in porosity. The maximum initial

SATHER ET AL. 8 of 16

19447973, 2023, 2. Downloaded from https://agupubs.onlinelibrary.wiley.com/doi/10.10292022WR032943 by University Of Colorado, Wiley Online Library on [06/02/2023]. See the Terms and Condition

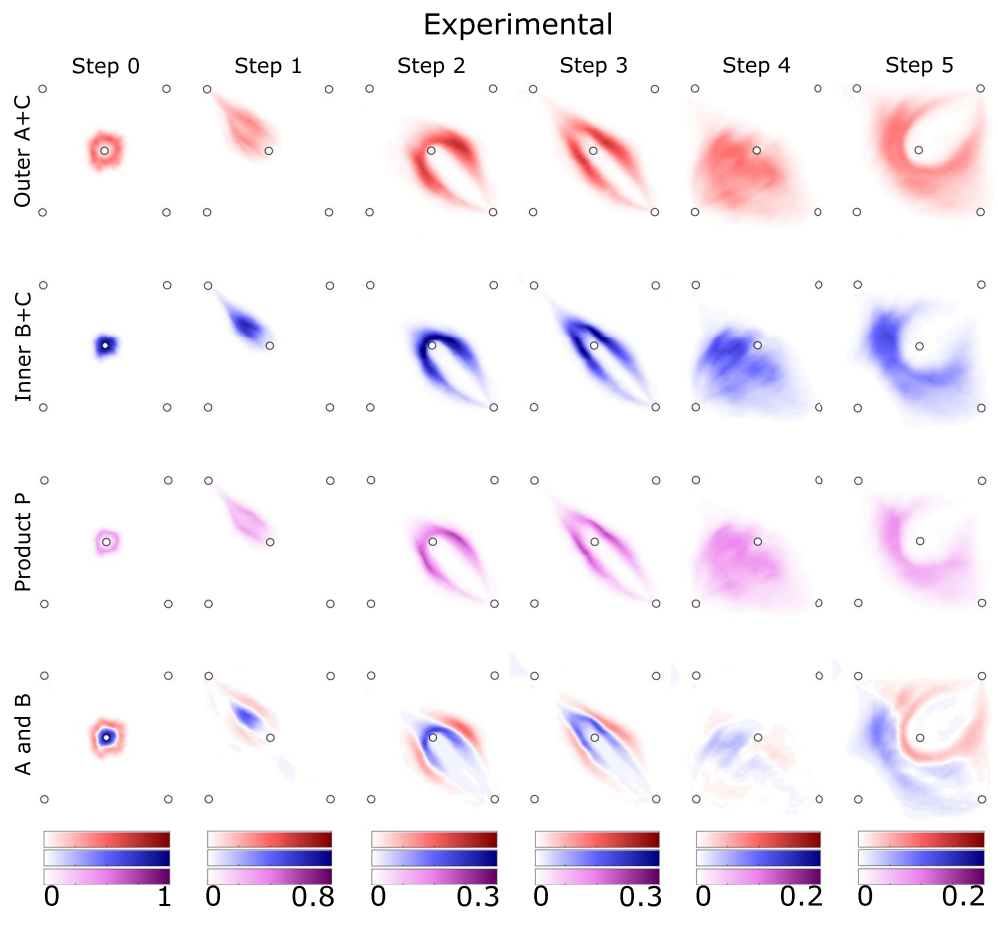


Figure 3. Plume spreading by the two-solute folding sequence. Experimental (top) and numerical (bottom) plume images of C/C_o for solute A, solute B, and the reaction product solute P. Open white circles represent wells (refer to Figure 1 for spatial scale).

concentration is nearly equal to the concentration of injected dye, C_o , which was determined from the constant dye concentrations in the pore flood experiment used to create the porosity map. This concentration was the same in each experiment, and is used to nondimensionalize results as C/C_o .

Using well numbers from Figure 1, after step 1, the plume has been stretched toward the northwest, using a dipole from well W2 to well W4. After step 2, the plume has been folded around the center well, using a dipole from W4 to W2, superimposed with a second dipole from W5 to W2, such that the center well W5 acts like a fulcrum. After step 3, the plume has been elongated by injecting through opposite wells W1 and W3 while extracting from W2 and W4. After step 4, the plume has been shifted toward the southwest, using a dipole from W1 to W3, and then finally after step 5 the plume has been folded for a second time around the center well using dipoles from W3 to W1 and from W5 to W1. After step 5, the two replicates are visually identical, consistent with a high spatial correlation of $\rho = 0.99$ (Table 4), and correlations above $\rho = 0.99$ for all other steps. These results confirm that the experimental protocol is highly reproducible. The numerical results differ from the experimental results, but only slightly. When compared against Experiment 2, for which the numerical initial condition was matched, a slightly lower spatial correlation of $\rho = 0.96$ was measured for step 5, with all other steps having correlation above $\rho = 0.95$.

Results for the folding two-solute sequence are shown in Figure 3, where the first row shows the experimentally-measured concentration of solute A + P, representing the remediation amendment injected into the contaminant plume; the second row shows the experimentally-measured concentration of solute B + P, representing the contaminant plume after injection of the remediation amendment; the third row shows the numerically-simulated reaction product P, and the fourth row shows the numerically simulated plumes of A

SATHER ET AL. 9 of 16

1947973, 2023, 2. Downloaded from https://agupubs.onlinelibrary.wiley.com/doi/10.1029/2022WR032943 by University Of Colorado, Wiley Online Library on [06/02/2023]. See the Terms and Conditions

are governed by the applicable Creative Co

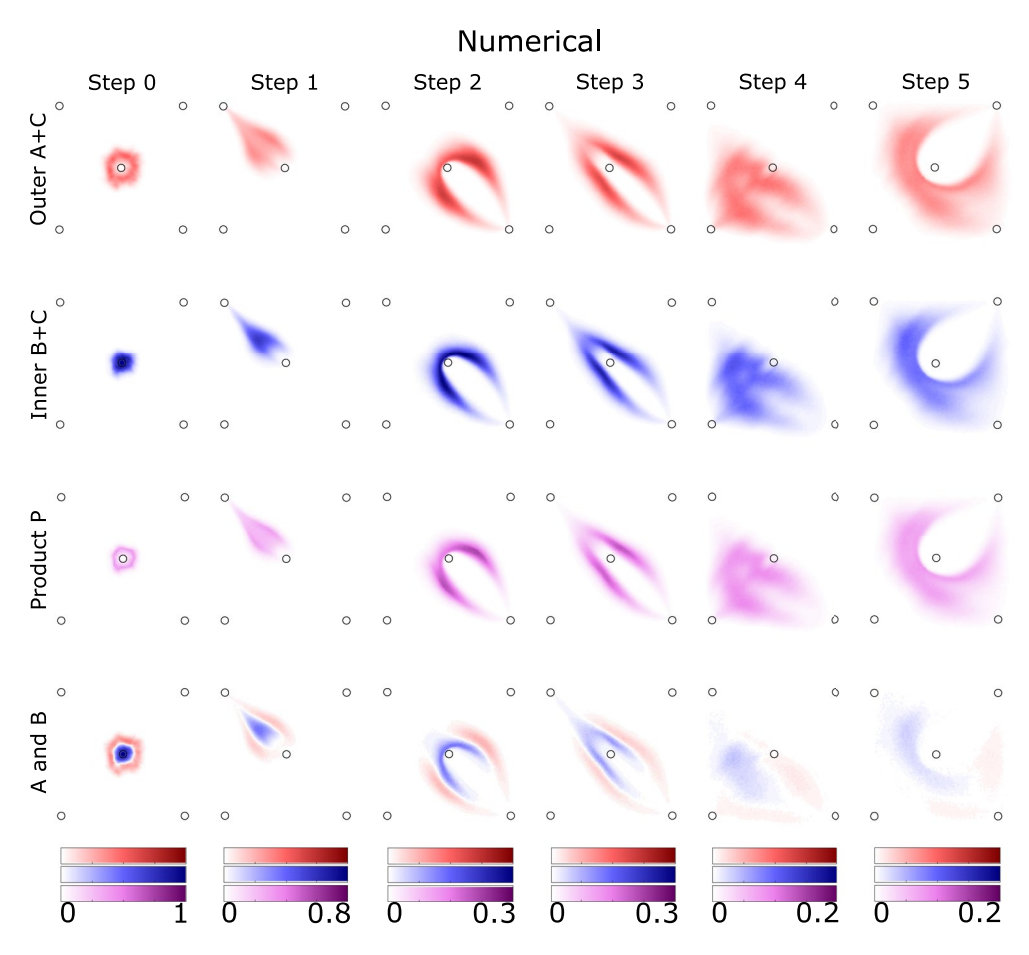


Figure 3. (Continued)

and B, where the assumption of instantaneous reaction (infinite Damköhler number) ensures that the plumes never overlap. Both solute A and solute B follow the pumping sequence of Table 1 as discussed above. There is a striking qualitative similarity between the plumes of reaction product and the individual plumes of solute A or solute B, or indeed the plumes of non-reactive solute shown in Figure 2. This result reinforces the simple notion that reaction takes place exclusively where reactants mix, that is, where they are close enough to allow molecule-to-molecule contact resulting from diffusion. Again, numerical results have high spatial correlation with the experimental results, with all $\rho \geq 0.84$ and most $\rho \geq 0.94$ (Table 5).

Experimental and simulation results for the oscillating sequence (Table 2) are shown in Figure 4. Once again using well numbers from Figure 1, after step 1, the plume has been enlarged to a ring by injecting through the center well W5 while extracting from W2 and W4. After step 2, the plume has been stretched from northwest to southeast using superimposed dipoles from W1 to W2 and from W3 to W4. These first two steps have stretched the plume to elongate its interface. The next three steps deliberately create velocity perpendicular to this elongated interface, first with a dipole from W3 to W1 (step 3), then with a dipole from W1 to W3 (step 4), and again

Table 5Correlation Coefficients for Two-Solute Simulations and Experiments of Reactive Transport

	Initial condition	Step 1	Step 2	Step 3	Step 4	Step 5
Contaminant Plume $A + P$ Experiment versus Numerical	1.00	0.97	0.94	0.97	0.96	0.94
Amendment Plume $B + P$ Experiment versus Numerical	1.00	0.95	0.86	0.91	0.94	0.84
Product Plume P Experiment versus Numerical	1.00	0.96	0.88	0.93	0.95	0.91

SATHER ET AL. 10 of 16

19447973, 2023, 2, Downloaded from https://agupubs.

onlinelibrary.wiley.com/doi/10.1029/2022WR032943 by University Of Colorado, Wiley

Figure 4. Experimental and numerical plume images of C/C_o for the oscillating sequence. Red circles indicate wells (refer to Figure 1 for spatial scale).

with a second dipole from W3 to W3 (step 5). The experimental and simulation results in Figure 4 are similar to each other, having a spatial correlation above $\rho = 0.96$ for all steps (Table 4).

A comparison of total mass and mass reacted between experiments and numerical simulations are shown in Figure 5. For non-reactive transport, total mass, M_T , at the conclusion of each pumping step is normalized by total mass at step 0, M_{T_0} . Similarly for reactive transport, total mass for each solute A, B, or product P, M_{i_0} are also normalized by the total mass of all solutes at step 0, M_{To} . For non-reactive transport, differences in total mass between experiments and simulations (Figure 5a) stay near 6% for the oscillating sequence, resulting from an experimental artifact, specifically residual dye in W5 after the initial dye injection, which added relatively more mass to the experiments in Step 1. The folding experiments showed an increase of 8% over simulations during step 2 due to the injection of residual dye from the center well and from excessive dye extraction from the surrounding wells in the numerical simulations. Two-solute experiments and simulations (Figure 5b) showed greater agreement than the non-reactive transport scenario for all steps because particles were at the center well during Step 1 of the numerical simulations. The differences in total mass between the experiment and simulation are near 5% for A + P and B + P. Reaction product P shows similar agreement during steps 1–4, but has a significant difference of over 20% during step 5. The greater difference at step 5 comes from an aspect of physics of the experimental system that cannot be simulated numerically. Specifically, because molecular diffusion of Rhodamine dye in glycerin is negligible within the time scale of the experiment (Roth et al., 2021), spreading of dye can be reversed during flow reversal (Neupauer et al., 2021). Since the experimental results infer the concentration of the reaction product from the overlapping of the plumes of non-reactive solutes A + P and B + P, the experimentally observed reversed spreading of these non-reactive solutes leads to a spurious numerically modeled reversal of reaction as well, which is not realistic. Thus, this is a limitation of the two-solute approach to mimic reactive transport. The reversal of reaction is not observed in the numerical simulations because spreading cannot be reversed in a traditional random walk method (Neupauer et al., 2021); thus the numerical simulations show more reaction than the experiments. These differences in experimentally observed and numerically simulated total mass do not, however, diminish the two-dimensional correlation coefficients between experimentally observed and numerically simulated spatial patterns (Table 4, Table 5). This is because the two-dimensional correlation, defined in Equation 11, is based on deviations from mean concentrations; differences in mean concentrations would therefore change the total mass but not the two-dimensional correlation, the latter of which reflects the plume geometry.

4. Discussion

The simulations and experiments presented here (a) provide a new window through which to measure how solute plumes interact in porous media, (b) demonstrate a novel experimental method to mimic reactive transport in the high-Damköhler limit, and (c) illustrate how reactive transport depends on the interaction of velocity fields, plume interfaces, and longitudinal and transverse hydrodynamic dispersion. Let us consider each of these points.

SATHER ET AL. 11 of 16

19447973, 2023, 2, Download

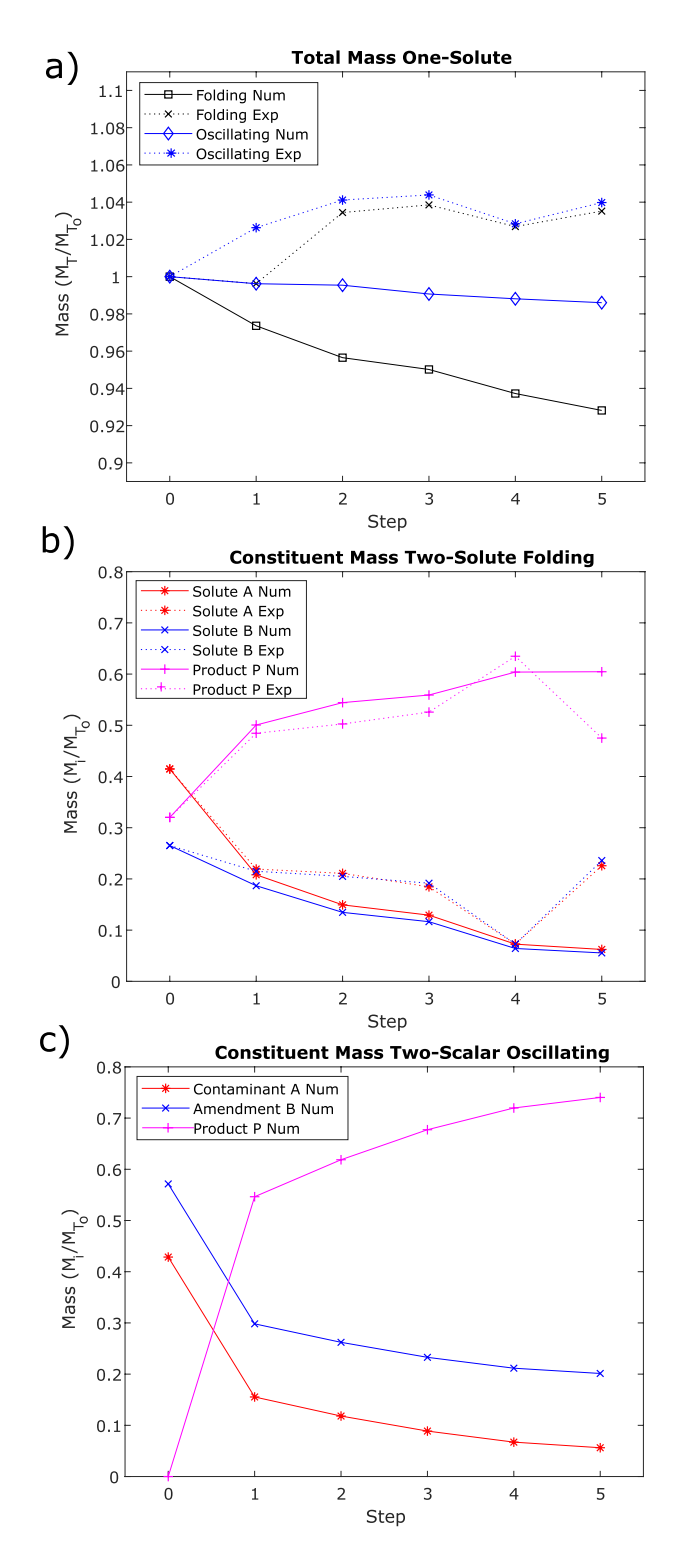


Figure 5. Non-dimensional total mass versus pumping step. (a) Single-solute experiments and simulations of non-reactive transport for folding and oscillating sequences. For the folding sequence, experimental results average two replicates. (b) Two-solute experiments and simulations of reactive transport for the folding sequence. (c) Two-solute simulation of reactive transport for the oscillating sequence, which did not have a corresponding experiment.

First, the experiments presented here provide an important way to validate model results, and to generate new observations to motivate future modeling efforts. For several decades, the research community has accepted that so-called anomalous transport, that is, transport differing from that predicted with a conventional Fickian model of hydrodynamic dispersion, is common in actual porous media. So common, in fact, that the phrase anomalous transport is a misnomer. The community has developed a host of modeling approaches to conceptualize hydrodynamic dispersion more realistically, including diffusion-limited transport from contaminated zones of immobile water or low permeability (Haggerty & Gorelick, 1995), incomplete mixing at the pore scale (Le Borgne et al., 2011; Scheibe et al., 2015), and chaotic advection (Lester et al., 2013). The experiments presented here provide a new window through which to measure how solute plumes interact in porous media. For example, although there was some evidence of non-radial flow resulting from imperfect bead packing, we observed no evidence of preferential channeling resulting from the hexagonal close packing of spherical media, at least when observed at the Darcy scale (i.e., averaged over many pore volumes). The experimental apparatus described here could easily be modified to accept a variety of porous media or source-sink configurations. In addition, the apparatus could be used to model mixing processes involving numerous solutes. Future applications would need to provide due attention to a number of limitations inherent in the experimental design. First, while refractive index matching with glass beads in glycerin provides a nontoxic combination, it comes bundled with a low molecular diffusion coefficient (compared to solutes in water) that could make actual reactive transport experiments time consuming. Second, it would be necessary to identify a model reaction $A + B \rightarrow P$ whose reaction product P not only avoids clogging but also avoids interference with the refractive index matching. But if one accepts, as a premise, that reactions in porous media are transport-limited, then the apparatus presented here provides a pathway for new experiments explicitly focused on transport.

Second, the experiments presented here demonstrate a novel method to generate data that can be used to simulate reactive transport in the high-Damköhler limit, that is, where the rate of reaction is much larger than the rate of transport, such that chemical transformations are transport-limited, which is the usual expectation for subsurface reactive transport (e.g., Kitanidis, 2012). To be clear, the folding sequence with two solutes (Table 1) has no reaction so its Damköhler number is zero as in other non-reactive experiments (e.g., Wang et al., 2022). Rather this approach is a simulation of transport-limited reaction, corresponding to the high-Damköhler number limit, based on experimental measurements of sequentially-injected plumes (Figure 6). In other words, this approach is based on the premise that reactive transport will be controlled, almost entirely, by how the two plumes mix. Adopting this approach allows one to focus on the hydrodynamic aspects of reactive transport, because it avoids the two limitations stated above: (a) actual reactions might generate permeability alterations, and therefore complicate the velocity field, and (b) actual reactions might compromise the refractive index match between the fluid and the granular media, and therefore preclude the measurement of pore-scale plume dispersion. In other words, stripping away the effects of reaction itself allows one to focus on transport. This simplification permits focus on the fundamental hydrodynamics, that is, non-reactive transport, an advance made possible by sequential plume injection into RIM matched porous media.

SATHER ET AL. 12 of 16

19447973, 2023, 2, Downloaded from https://agupub

rary.wiley.com/doi/10.1092/022WR032943 by University Of Colorado, Wiley Online Library on [06/02/2023]. See the Terms and Conditions (https://onlinelibrary.wiley.com/terms-and-conditions) on Wiley Online Library for rules of use; OA articles are governed by the applicable Creative Commons License

Figure 6. Schematic of superposition of two solutes to mimic reactive transport. Solute A (red) is imaged separately from solute B (blue). When the two images are combined, the overlapping area of the solutes indicates reaction product P (purple). This method assumes a high Damköhler number. Black circles indicate well locations.

Third, numerically-simulated reaction during the oscillating sequence (Table 2) illustrates how reactive transport depends on the interaction of velocity fields, plume interfaces, and longitudinal and transverse hydrodynamic dispersion. It is widely recognized that transverse dispersion is often the transport-limiting factor in subsurface reactive transport (Cirpka et al., 2011), because plumes deformed under steady flow stretch during advection through high-permeability zones, which amplifies the relative importance of transport transverse to the local velocity field (i.e., transverse dispersion) compared to transport across the leading or trailing edges of the plume (i.e., longitudinal dispersion). In the special case of quasi-two dimensional radial flow from a well, it is possible to derive semi-analytical expressions for the relative contributions of pore-scale mixing and mechanical dispersion precisely because the plume interface is always perpendicular to the radial flow direction (Neupauer et al., 2020). Indeed, in the case of

reversible radial flow, there is evidence that dispersion itself is reversible, reflecting incomplete mixing within pores (Neupauer et al., 2021).

EIE introduces the possibility of deliberately manipulating the velocity field to achieve certain objectives. In the case of groundwater remediation, the objective is to maximize contaminant degradation. For example, Di Dato et al. (2018) derived a semi-analytical solution, subject to certain simplifying assumptions, for the temporal evolution of Kitanidis's (1994) dilution index for a plume manipulated by EIE in a heterogeneous aquifer. Their solution showed that EIE works in tandem with heterogeneity to amplify mixing through both longitudinal and transverse dispersion. Recognizing that longitudinal dispersion is generally much larger than transverse

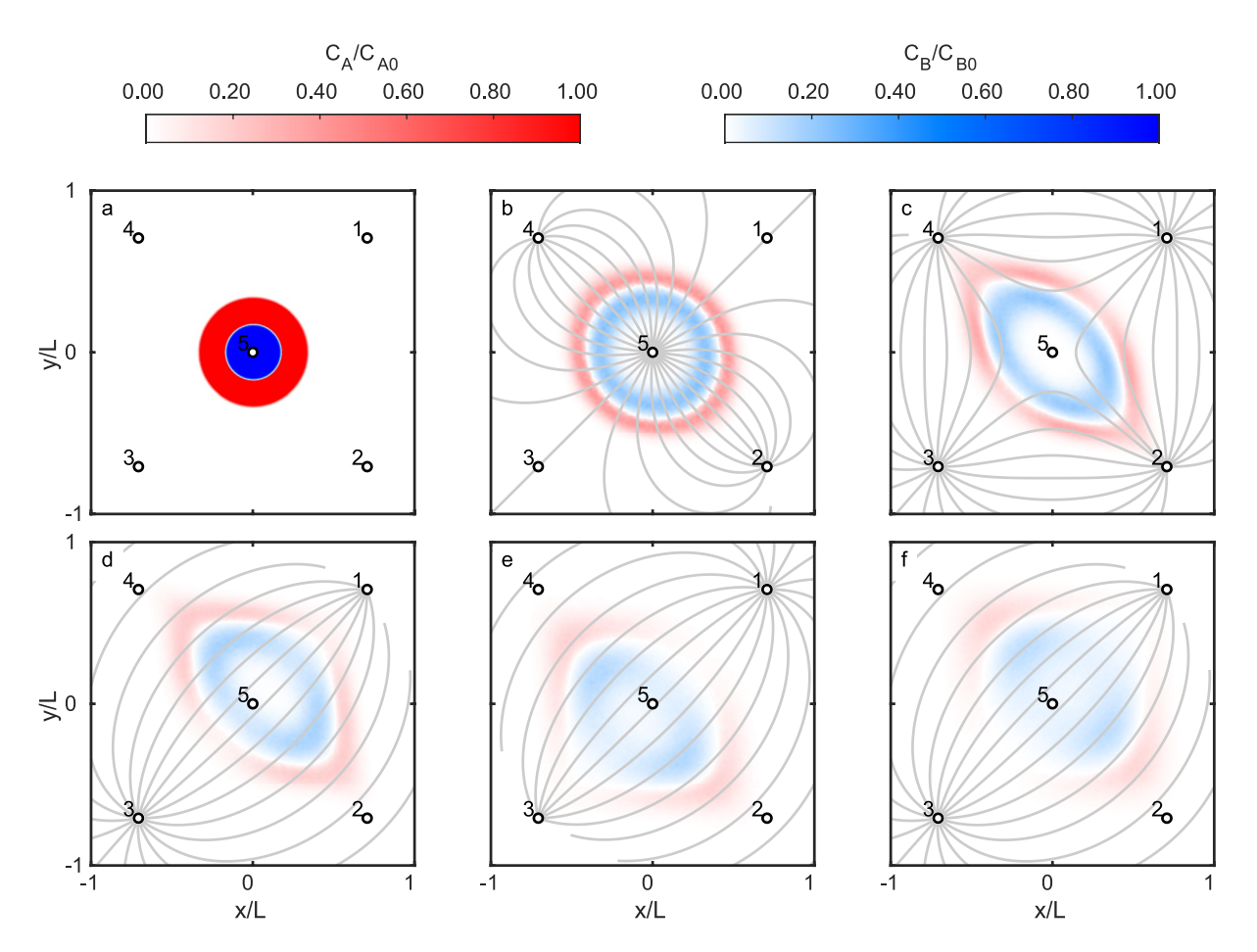


Figure 7. Simulated plumes of contaminant *A* (red) and amendment *B* (blue) with the oscillating sequence for (a) Initial condition; (b) at the end of Step 1; (c) at the end of Step 2; (d) at the end of Step 3; (e) at the end of Step 4; and (f) at the end of Step 5. Gray lines are streamlines. Open white circles represent wells.

SATHER ET AL. 13 of 16

dispersion (i.e., by one order of magnitude), one strategy is to manipulate the plume to maximize its interfacial area, and then to manipulate the velocity field to make streamlines generally perpendicular to the plume interface (Sather et al., 2022). This is exactly the rationale behind the oscillating sequence, where steps 1–2 stretch the initially circular plume into an ellipse, and steps 3–5 impose dipole velocity fields, in alternating directions, such that the plume oscillates around its initial position with the velocity field generally perpendicular to its interface (Figure 7). Figures 7d–7f clearly shows that the contaminant concentration decreases more rapidly where the streamlines are perpendicular to the plume interface (northeast and southwest), as compared to where streamlines are tangent to the plume interface (northwest and southeast). Numerical simulations of reactive transport (Figure 5) show that this strategy is effective, evidenced by increased contaminant degradation (beyond that provided by the initial condition) by the oscillating sequence compared to the folding sequence (compare Figures 5b and 5c).

While our previous work on EIE focused on a certain 12-step pumping sequence designed to generate chaotic advection (Mays & Neupauer, 2012), this study explored two alternative sequences designed to emphasize contaminant degradation. The folding sequence was designed following Ottino's (1989) stretching-and-folding recipe for chaotic advection, but it turned out to generate slower simulated contaminant degradation than the oscillating sequence. Nevertheless, the folding sequence provided a test bed to demonstrate a novel technique to mimic reactive transport in the high-Damköhler limit. The oscillating sequence was designed to make the flow velocity generally perpendicular to the plume interface, which resulted in more complete degradation of the simulated contaminant than the folding sequence during steps 1 through 5. Either of these pumping sequences is more practical than the previously-studied 12-step sequence, because they have only five steps, and require fewer pore volumes of fluid to be injected and extracted: The 12-step sequence required total pumping, including both injection and extraction, of 8.9 pore volumes, while the folding sequence required 3.6 pore volumes, and the oscillating sequence required only 1.6 pore volumes. And, because they are strictly net-zero-injection sequences, they require no above-ground tank to store any injection-extraction imbalance.

5. Conclusions

The promise of EIE is that one can design a velocity field to partially overcome the fundamental constraint that reaction in porous media is transport-limited. Previous simulations have explored this promise (Bagtzoglou & Oates, 2007; Mays & Neupauer, 2012; Sposito, 2006), and previous experiments have been reported (Cho et al., 2019; Zhang et al., 2009). The current work advances these simulations and experiments by offering a comprehensive experimental protocol for studying EIE with refractive index matching (Dijksman et al., 2012) and laser-induced fluorescence (Crimaldi, 2008), adapting these methods for plume spreading (Roth et al., 2021), and implementing new techniques to mitigate wall effects (Roth et al., 2020). The experimental apparatus design proved itself over the course of this research, and now that its efficacy has been shown, it could be used for further investigation of fluid dynamics within porous media systems.

Comparison of simulations and experiments reveals both similarities and differences. Spatial distributions of solutes between experimental replicates are practically identical, based on their high spatial correlation (Roth et al., 2021). Similarly, spatial distributions of solutes between simulations and experiments are also highly correlated, which validates the numerical modeling approach. This validation provides a foundation for additional simulations on EIE, beyond the scope of this work, that are reported elsewhere (Sather et al., 2022). Differences between experiments and simulations are most notable during stretching events when concentration gradients are being sharpened. Here the Fickian model becomes less accurate due to unmixing in the minimally diffusive experimental environment.

Taken together, comparing and contrasting these two pumping sequences has demonstrated the advantages and disadvantages of various approaches for designing pumping sequences. Framing this work in the context of design is important, since our ultimate goal is to design EIE sequences that support improved remediation of contaminated groundwater by overcoming the transport limitations inherent to chemical transformations in the subsurface. In this light, the simulations and experiments reported provide a foundation for field testing.

SATHER ET AL. 14 of 16

Data Availability Statement

Experimental data are available through HydroShare at https://doi.org/10.4211/hs.4b8575d3031c40d4a39f945d-b8f02ae5. Simulations used Matlab R2019b for Linux, MODFLOW-2005 (Harbaugh et al., 2017), RW3D (Salamon et al., 2006), and the R package locfit (Loader, 2013). Matlab scripts and model input files are also available through HydroShare at https://doi.org/10.4211/hs.4b8575d3031c40d4a39f945db8f02ae5.

Acknowledgments

The authors thank Danielle Szafir for collegial assistance, three anonymous referees for their specific and constructive reviews, and the U.S. National Science Foundation for funding through awards EAR-1417005 and EAR-1417017.

References

- Aref, H., Blake, J. R., Budisic, M., Cardoso, S. S. S., Cartwright, J. H. E., Clercx, H. J. H., et al. (2017). Frontiers of chaotic advection. *Reviews of Modern Physics*, 89(2), 025007. https://doi.org/10.1103/RevModPhys.89.025007
- Asha Farsana, M., Sajikumar, N., & Subaida, E. A. (2021). Three-dimensional investigation of engineered injection and extraction for enhanced groundwater remediation. *Journal of Hydrologic Engineering*, 26(8), 04021028. https://doi.org/10.1061/(ASCE)HE.1943-5584.0002114
- Bagtzoglou, A. C., & Oates, P. M. (2007). Chaotic advection and enhanced groundwater remediation. *Journal of Materials in Civil Engineering*, 19(1), 75–82. https://doi.org/10.1061/(ASCE)0899-1561(2007)19:1(75)
- Berkowitz, B., Cortis, A., Dentz, M., & Scher, H. (2006). Modeling non-Fickian transport in geological formations as a continuous time random walk. Reviews of Geophysics, 44(2). https://doi.org/10.1029/2005rg000178
- wark. Reviews of Geophysics, 44(2). https://doi.org/10.1029/2005rg000178

 Cha, K. Y., & Borden, R. C. (2012). Impact of injection system design on ISCO performance with permanganate—Mathematical modeling
- results. Journal of Contaminant Hydrology, 128(1-4), 33-46. https://doi.org/10.1016/j.jconhyd.2011.10.001
 Cho, M. S., Solano, F., Thomson, N. R., Trefry, M. G., Lester, D. R., & Metcalfe, G. (2019). Field trials of chaotic advection to enhance reagent
- delivery. Ground Water Monitoring and Remediation, 39(3), 23–39. https://doi.org/10.1111/gwmr.12339
 Cirpka, O. A., de Barros, F. P. J., Chiogna, G., Rolle, M., & Nowak, W. (2011). Stochastic flux-related analysis of transverse mixing in two-di-
- mensional heterogeneous porous media. Water Resources Research, 47(6), W06515. https://doi.org/10.1029/2010WR010279
 Crimaldi, J. P. (2008). Planar laser induced fluorescence in aqueous flows. Experiments in Fluids, 44(6), 851–863. https://doi.org/10.1007/
- Crimaldi, J. P. (2008). Planar laser induced fluorescence in aqueous flows. Experiments in Fluids, 44(6), 851–863. https://doi.org/10.1007/s00348-008-0496-2
- Di Dato, M., de Barros, F. P. J., Fiori, A., & Bellin, A. (2018). Improving the efficiency of 3-D hydrogeological mixers: Dilution enhancement via coupled engineering-induced transient flows and spatial heterogeneity. Water Resources Research, 54(3), 2095–2111. https://doi.org/10.1002/2017WR022116
- Dijksman, J. A., Rietz, F., Lörincz, K. A., van Hecke, M., & Losert, W. (2012). Refractive index matched scanning of dense granular materials. Review of Scientific Instruments, 83(1), 011301. https://doi.org/10.1063/1.3674173
- Gramling, C., Harvey, C., & Meigs, L. (2002). Reactive transport in porous media: A comparison of model prediction and laboratory visualization. *Environmental Science and Technology*, 36(11), 2508–2514. https://doi.org/10.1021/es0157144
- Haggerty, R., & Gorelick, S. M. (1995). Multiple-rate mass transfer for modeling diffusion and surface reactions in media with pore-scale heterogeneity. Water Resources Research, 31(10), 2383–2400. https://doi.org/10.1029/95WR01583
- Harbaugh, A. W., Langevin, C. D., Hughes, J. D., Niswonger, R. N., & Konikow, L. F. (2017). MODFLOW-2005 version 1.12.00, the U.S. Geological Survey modular groundwater model: US Geological Survey software release. USGS. https://doi.org/10.5066/F7RF5S7G
- Jones, S. W., & Aref, H. (1988). Chaotic advection in pulsed source sink systems. Physics of Fluids, 31(3), 469–485. https://doi.org/10.1063/ 1.866828
- Jose, S. C., & Cirpka, O. A. (2004). Measurement of mixing-controlled reactive transport in homogeneous porous media and its prediction from
- conservative tracer test data. Environmental Science and Technology, 38(7), 2089–2096. https://doi.org/10.1021/es034586b Kitanidis, P. K. (1994). The concept of the dilution index. Water Resources Research, 30(7), 2011–2026. https://doi.org/10.1029/94WR00762
- Kitanidis, P. K. (2012). Transport and mixing, chapter 3. In P. K. Kitanidis & P. L. McCarty (Eds.), Delivery and mixing in the subsurface: Processes and design principles for in situ remediation, SERDP ESTCP environmental remediation technology (Vol. 4). Springer. https://doi.org/10.10 07/978-1-4614-2239-6_3
- Le Borgne, R., Dentz, M., Davy, P., Bolster, D., Carrera, J., de Dreuzy, J.-R., & Bour, O. (2011). Persistence of incomplete mixing: A key to anomalous transport. *Physical Review*, 84(1), 015301. https://doi.org/10.1103/PhysRevE.84.015301
- Le Borgne, T., Dentz, M., Bolster, D., Carrera, J., de Dreuzy, J. R., & Davy, P. (2010). Non-Fickian mixing: Temporal evolution of the scalar dissipation rate in heterogeneous porous media. Advances in Water Resources, 33(12), 1468–1475. https://doi.org/10.1016/j.advwatres.2010.08.006
- Le Borgne, T., Dentz, M., & Carrera, J. (2008a). Lagrangian statistical model for transport in highly heterogeneous velocity fields. *Physical Review Letters*, 101(9), 090601. https://doi.org/10.1103/physrevlett.101.090601
- Le Borgne, T., Dentz, M., & Carrera, J. (2008b). Spatial Markov processes for modeling Lagrangian particle dynamics in heterogeneous porous media. *Physical Review*, 78(2), 026308. https://doi.org/10.1103/physreve.78.026308
- Lester, D., Metcalfe, G., Trefry, M. G., Ord, A., Hobbs, B., & Rudman, M. (2009). Lagrangian topology of a periodically reoriented potential flows: Symmetry, optimization, and mixing. *Physical Review*, 80(3), 036298. https://doi.org/10.1103/PhysRevE.80.036208
- Lester, D. R., Metcalfe, G., & Trefry, M. G. (2013). Is chaotic advection inherent to porous media flow? *Physical Review Letters*, 111(17), 174101. https://doi.org/10.1103/PhysRevLett.111.174101
- Loader, C. (2013). locfit: Local regression, likelihood and density estimation. R package version 1.5-9.1. Retrieved from https://cran.r-project.org/web/packages/locfit/locfit.pdf
- Mays, D. C., & Neupauer, R. M. (2012). Plume spreading in groundwater by stretching and folding. *Water Resources Research*, 48(7), W07501. https://doi.org/10.1029/2011WR011567
- Mays, D. C., & Neupauer, R. M. (2013). Reply to comment on "Plume spreading in groundwater by stretching and folding". Water Resources Research, 49(2), 1192–1194. https://doi.org/10.1029/2012WR013129
- Meile, C., & Scheibe, T. D. (2019). Reactive transport modeling of microbial dynamics. *Elements*, 15(2), 111–116. https://doi.org/10.2138/gselements.15.2.111
- Neupauer, R. M., & Mays, D. C. (2015). Engineered injection and extraction for in situ remediation of sorbing solutes in groundwater. *Journal of Environmental Engineering*, 141(6), 040140951. https://doi.org/10.1061/(ASCE)EE.1943-7870.0000923
- Neupauer, R. M., Meiss, J. D., & Mays, D. C. (2014). Chaotic advection and reaction during engineered injection and extraction in heterogeneous porous media. Water Resources Research, 50(2), 1433–1447. https://doi.org/10.1002/2013WR014057
- Neupauer, R. M., Roth, E. J., Crimaldi, J. P., Mays, D. C., & Sather, L. J. (2021). Demonstration of reversible dispersion in a Darcy-scale push-pull laboratory experiment. Transport in Porous Media. https://doi.org/10.1007/s11242-021-01682-3

SATHER ET AL. 15 of 16

- Neupauer, R. M., Sather, L. J., Mays, D. C., Crimaldi, J. P., & Roth, E. J. (2020). Contributions of pore-scale mixing and mechanical dispersion to reaction in radial groundwater flow. *Water Resources Research*, 56(7), e2019WR026276. https://doi.org/10.1029/2019WR026276
- Ottino, J. M. (1989). The kinematics of mixing: Stretching, chaos, and transport. Cambridge University Press.
- Piscopo, A. N., Kasprzyk, J. R., & Neupauer, R. M. (2015). An iterative approach to multi-objective engineering design: Optimization of engineered injection and extraction for enhanced groundwater remediation. *Environmental Modelling & Software*, 69, 253–261. https://doi.org/10.1016/j.envsoft.2014.08.030
- Piscopo, A. N., Neupauer, R. M., & Kasprzyk, J. R. (2016). Optimal design of active spreading systems to remediate sorbing groundwater contaminants in situ. *Journal of Contaminant Hydrology*, 190, 29–43. https://doi.org/10.1016/j.jconhyd.2016.03.005
- Piscopo, A. N., Neupauer, R. M., & Mays, D. C. (2013). Engineered injection and extraction to enhance reaction for improved in situ remediation. Water Resources Research, 49(6), 3618–3625. https://doi.org/10.1002/wrcr.20209
- Reising, L. J. (2018). Effects of active and passive spreading on mixing and reaction during groundwater remediation by engineered injection and extraction. Doctoral dissertation, Department of Civil, Environmental, and Architectural Engineering, University of Colorado Boulder.
- Rodríguez-Escales, P., Fernàndez-Garcia, D., Dreschel, J., Folch, A., & Xanchez-Vila, X. (2017). Improving degradation of emerging organic compounds by applying chaotic advection in managed aquifer recharge in randomly heterogeneous porous media. *Water Resources Research*, 53(5), 4376–4392. https://doi.org/10.1002/2016WR020333
- Roth, E. J. (2018). Experimental investigation of scalar spreading by engineered injection and extraction in porous media. Doctoral dissertation, Department of Civil, Environmental, and Architectural Engineering, University of Colorado Boulder.
- Roth, E. J., Mays, D. C., Neupauer, R. M., Sather, L. J., & Crimaldi, J. P. (2021). Methods for laser-induced fluorescence imaging of solute plumes at the Darcy scale in quasi-two-dimensional, refractive index-matched porous media. Transport in Porous Media. https://doi.org/10.1007/ s11242-021-01545-x
- Roth, E. J., Neupauer, R. M., Mays, D. C., Sather, L. J., & Crimaldi, J. P. (2020). Wall effect mitigation techniques for experiments with planar walls. Transport in Porous Media. https://doi.org/10.1007/s11242-020-01399-9
- Salamon, P., Fernandez-Garcia, D., & Gomez-Hernandez, J. J. (2006). Modeling mass transfer processes using random walk particle tracking. Water Resources Research, 42(11), W11417. https://doi.org/10.1029/2006wr004927
- Sanchez-Vila, X., Dentz, M., & Donado, L. D. (2007). Transport-controlled reaction rates under local non-equilibrium conditions. *Geophysical Research Letters*, 34(10), L10404. https://doi.org/10.1029/2007GL029410
- Sather, L. J., Neupauer, R. M., Mays, D. C., Crimaldi, J. P., & Roth, E. J. (2022). Active spreading: Hydraulics for enhancing groundwater remediation. *Journal of Hydrologic Engineering*, 27(5). https://doi.org/10.1061/(ASCE)HE.1943-5584.0002167
- Scheibe, T. D., Schuchardt, K., Agarwal, K., Chase, J., Yang, X., Palmer, B. J., et al. (2015). Hybrid multiscale simulation of a mixing-controlled reaction. Advances in Water Resources, 83, 228–239. https://doi.org/10.1016/j.advwatres.2015.06.006
- Speetjens, M., Metcalfe, G., & Rudman, M. (2021). Lagrangian transport and chaotic advection in three-dimensional laminar flows. *Applied*
- Mechanics Reviews, 73(3), 030801. https://doi.org/10.1115/1.4050701

 Sposito, G. (2006). Chaotic solute advection by unsteady groundwater flow. Water Resources Research, 42(6), W06D03. https://doi.org/10.
- 1029/2005WR004518
 Stöhr, M., Roth, K., & Jähne, B. (2003). Measurement of 3D pore-scale flow in index-matched porous media. *Experiments in Fluids*, 35(2),
- 159–166. https://doi.org/10.1007/s00348-003-0641-x Trefry, M. G., Lester, D. R., Metcalfe, G., & Wu, J. (2019). Temporal fluctuations and poroelasticity can generate chaotic advection in natural
- groundwater systems. Water Resources Research, 55(4), 3347–3374. https://doi.org/10.1029/2018WR023864
- Valocchi, A. J., Bolster, D., & Werth, C. J. (2019). Mixing-limited reactions in porous media. *Transport in Porous Media*, 130(1), 157–182. https://doi.org/10.1007/s11242-018-1204-1
- Villermaux, E. (2019). Mixing versus stirring. Annual Review of Fluid Mechanics, 51(1), 245–273. https://doi.org/10.1146/annurev-fluid-0105 18-040306
- Wang, Y., Fernàndez-Garcia, D., Sole-Mari, G., & Rodríguez-Escales, P. (2022). Enhanced NAPL removal and mixing with engineered injection and extraction. Water Resources Research, 58(4), e2021WR031114. https://doi.org/10.1029/2021WR031114
- Ye, Y., Zhang, Y., Lu, C., Xie, Y., & Luo, J. (2021). Effective chemical delivery through multi-screen wells to enhance mixing and reaction of solute plumes in porous media. Water Resources Research, 57(2), e2020WR028551. https://doi.org/10.1029/2020WR028551
- Zhang, P. F., DeVries, S. L., Dathe, A., & Bagtzoglou, A. C. (2009). Enhanced mixing and plume containment in porous media under time-dependent oscillatory flow. Environmental Science and Technology, 43(16), 6283–6288. https://doi.org/10.1021/es900854r

SATHER ET AL. 16 of 16